Supporting Information for Ultrathin single-Crystalline Bi_2S_3 nanosheets for high-Performance photodetectors

Jintao Gao[1,†], Hongyu Liu[2,†], Yue Zhang[2,†], Zhaoyu Pan[2], Huanghuang Cheng[3], Feng Zhuo[3], Peng Zhang[3], Songqing Hu[2], Xuegang Chen[3,4,5], Wenshuai Gao[6], Xue Liu[3], Yuxuan Jiang[1,3,*], Jingyue Wang[2,*]

[1]School of Physics, Anhui University, Hefei 230601, P. R. China

[2]Shandong Key Laboratory of Intelligent Energy Materials, School of Materials Science and Engineering, China University of Petroleum (East China), Qingdao 266580, P. R. China

[3]Center of Free Electron and Laser and High Magnetic Fields, Anhui University, Hefei 230601, Anhui, P. R. China

[4]State Key Laboratory of Opto-Electronic Information Acquisition and Protection Technology, Anhui University, Hefei 230601, Anhui, P. R. China

[5]Anhui Provincial Key Laboratory of Magnetic Functional Materials and Devices, Anhui University, Hefei, 230601, Anhui, P. R. China

[6]Institutes of Physical Science and Information Technology, Anhui University, Hefei 230601, China

†These authors contributed equally to this work

*Corresponding author. E-mails: jingyue_wang@upc.edu.cn, Yuxuan.Jiang@ahu.edu.cn

Section 1: Growth control of Bi_2S_3 nanosheets

As shown in Figure S1a-c, increasing the carrier gas flow rate from 80 to 100 sccm changed the Bi_2S_3 morphology from nanowires to nanosheets, and the size increased from 4 to 20 μm. However, at 120 sccm, the size decreased. This evolution can be qualitatively understood in terms of gas-phase mass transport[1]. The hydrodynamic boundary-layer thickness can be approximately expressed as

$$\delta(x)=4.64\sqrt{\frac{\mu x}{\rho v}}, \quad (1)$$

where ρ is the gas density, v is the flow velocity, μ is the viscosity, and x is the flow distance. As the flow rate increases, the boundary-layer thickness decreases, which facilitates precursor diffusion from the gas stream to the substrate surface and improves the deposition efficiency, thereby favoring the growth of larger crystals. Meanwhile, the enhanced precursor supply can also modify the relative growth rates along different crystallographic directions, contributing to the morphology transition from nanowires to nanosheets. However, when the flow rate is further increased to 120 sccm, the precursor residence time in the growth zone becomes too short, which reduces the effective surface reaction probability and local supersaturation. As a result, the crystal size decreases.

Figure S1d-f show that the crystal size first increases and then decreases with increasing temperature from 450 to 550 ℃, reaching a maximum at 500 ℃. This behavior can be understood from the competition between nucleation and surface diffusion during crystal growth. According to classical nucleation theory, the critical nucleation barrier satisfies

$$\Delta G \propto \frac{\gamma^3}{\Delta T \Delta G_v^2}, \quad (2)$$

and the diffusion coefficient follows an Arrhenius-type relation,

$$D=D_0 e^{\frac{-E_a}{RT}}, \quad (3)$$

where γ is the surface energy, ΔG_v is the volumetric Gibbs free-energy difference, E_a is the activation energy, and R is the gas constant. At low temperatures, the nucleation barrier ΔG is low, but the weak atomic diffusion (D) limits crystal growth. At relatively low temperatures, the diffusion of adsorbed species is weak, which limits surface migration and suppresses lateral crystal growth, resulting in small domains. As the temperature increases, both surface diffusion and reaction kinetics are enhanced, promoting the growth of larger Bi_2S_3 crystals. However, when the temperature exceeds 500 °C, precursor depletion and enhanced desorption or re-evaporation may reduce the effective growth rate, leading to smaller Bi_2S_3 domains.[2-6]

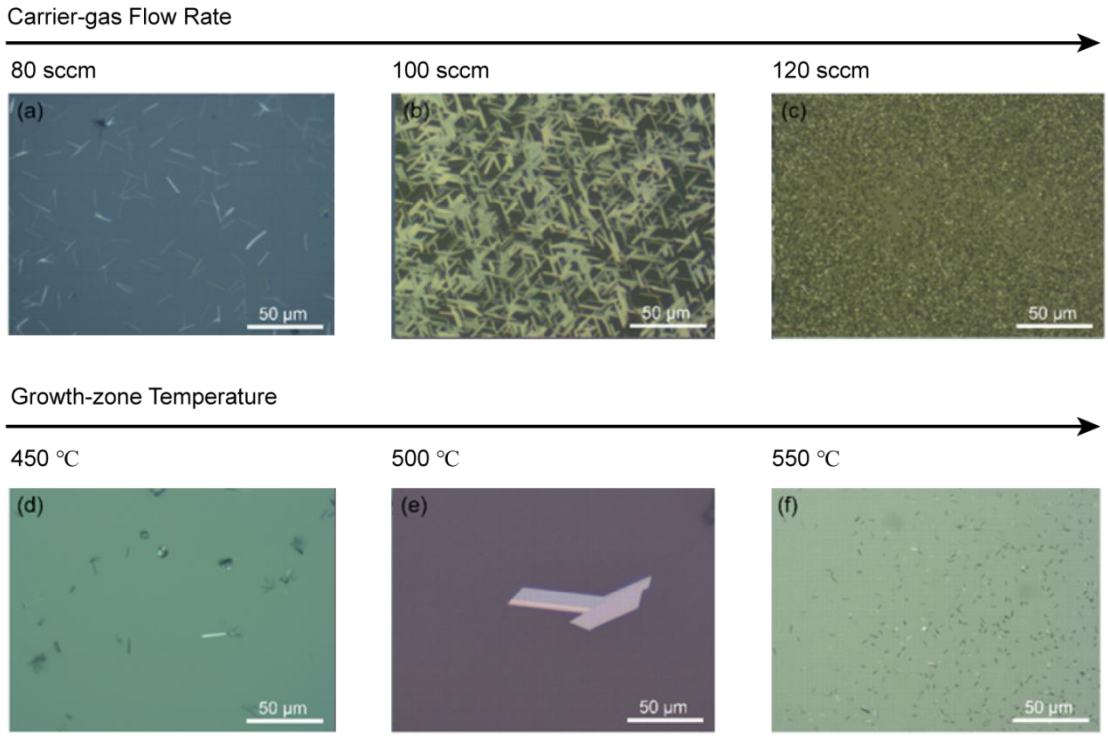

Figure S1. Growth-parameter optimization for LPCVD-grown two-dimensional Bi_2S_3. (a-c) Optical microscopy (OM) images acquired at a fixed temperature of 520 ℃ with carrier-gas flow rates of 80, 100, and 120 sccm, respectively. (d-f) OM images acquired at a fixed carrier-gas flow rate of 100 sccm with growth-zone temperatures of 450, 500, and 550 ℃, respectively.

Section 2: Further structural analysis of the as-grown Bi_2S_3 nanosheets

As shown in Figure S2a, scanning electron microscopy (SEM) was used to check the morphology of 2D Bi_2S_3 nanosheets grown on f-mica by the LPCVD method. Due to the anisotropic crystal growth, the nanosheets show regular rectangular shapes with very flat surfaces and no obvious structural damage. To further examine the elemental distribution, energy-dispersive X-ray spectroscopy (EDS) mapping was performed on an individual single-crystalline flake (Figures S2b and S2c). The Bi (green) and S (red) signals are uniformly distributed over the entire flake, with no noticeable local aggregation, indicating good compositional homogeneity. The corresponding EDS spectrum and quantitative analysis in Figure S2d reveal atomic percentages of 40.90% for Bi and 59.10% for S. The resulting S/Bi atomic ratio is approximately 1.44, which is close to the stoichiometric value of 1.50 for ideal Bi_2S_3. These results indicate that the LPCVD method enables the growth of high-quality 2D Bi_2S_3 crystals with near-stoichiometric composition and a low density of sulfur-vacancy-related defects.

To further evaluate the crystallographic quality of the as-grown Bi_2S_3 nanosheets, inverse fast Fourier transform (iFFT) analysis was performed on the high-resolution TEM images. As shown in Figure S3, clear and periodic lattice fringes are observed throughout the selected regions, corresponding to the (102) and (020) planes with interplanar spacings of approximately 0.324 and 0.548 nm, respectively. The continuity and uniformity of these lattice fringes over several nanometers confirm the high crystallinity of the nanosheets. No obvious lattice distortion, dislocation, or grain boundary is detected in either direction, indicating that the Bi_2S_3 flakes possess a well-ordered orthorhombic single-crystalline structure. These results further confirm the high crystalline quality of the Bi_2S_3 nanosheets grown by LPCVD. Such high crystal quality is expected to account for the ultrafast carrier transport and high mobility observed in the corresponding devices.

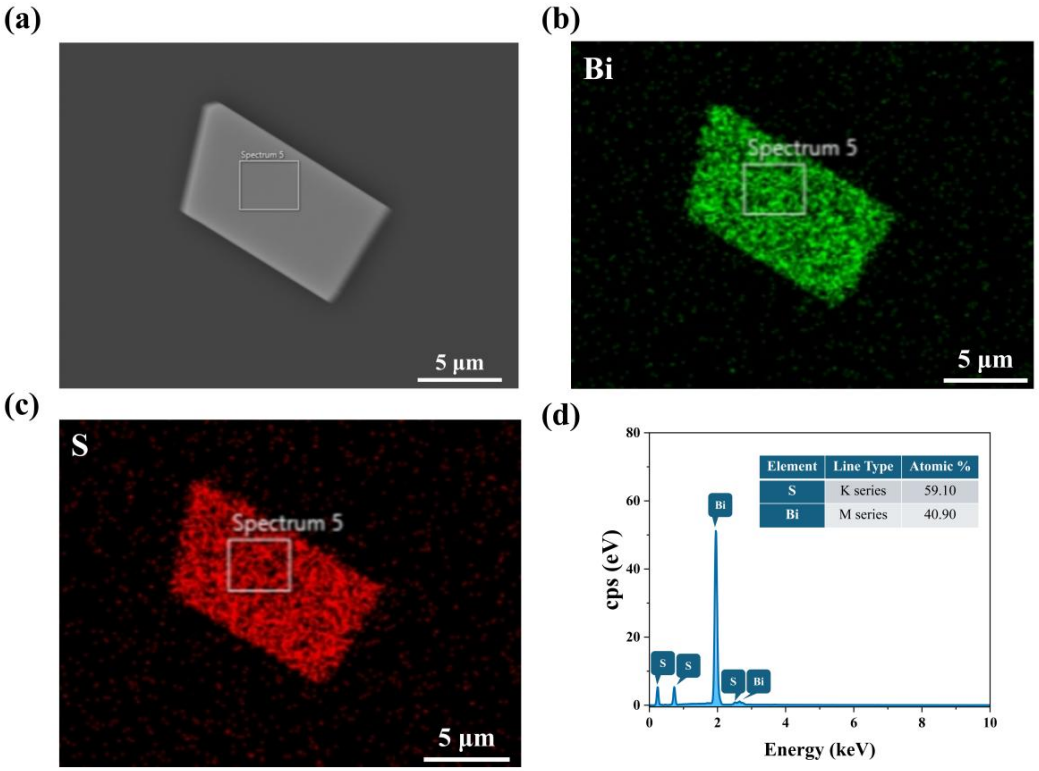

Figure S2. Morphological and compositional characterization of LPCVD-grown Bi_2S_3 nanosheets. (a) Field-emission scanning electron microscopy (SEM) image of a representative rectangular Bi_2S_3 nanosheet grown on fluorophlogopite mica (f-mica). (b,c) Energy-dispersive X-ray spectroscopy (EDS) elemental maps of (b) Bi (green) and (c) S (red) collected from the channel region, showing a spatially uniform elemental distribution across the entire flake. (d) EDS spectrum acquired from the selected region, with the inset table summarizing the quantitative atomic percentages of S and Bi.

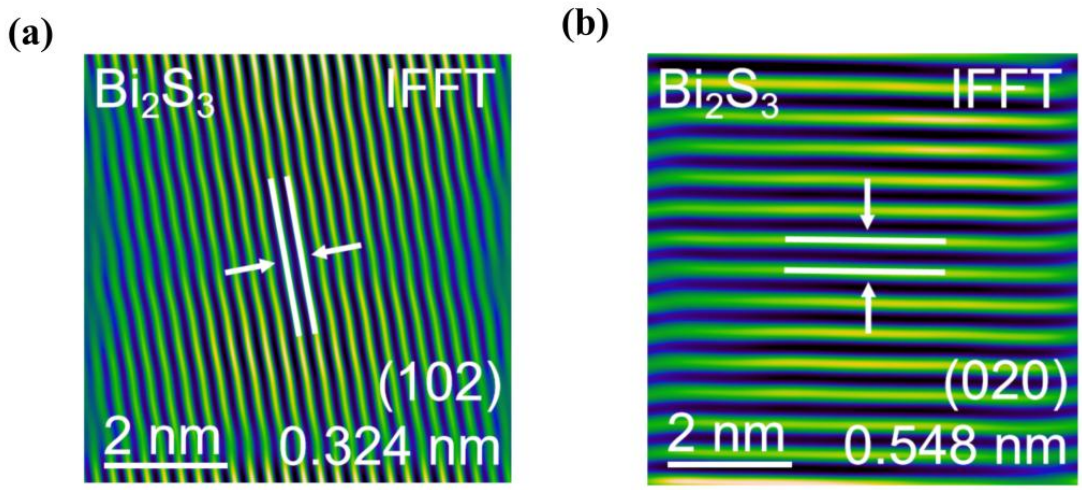

Figure S3. Inverse fast Fourier transform (iFFT) lattice images of two-dimensional Bi_2S_3 single crystals. (a) IFFT lattice fringes corresponding to the (102) family of planes, with an interplanar spacing of approximately 0.324 nm. (b) iFFT lattice fringes corresponding to the (020) family of planes, yielding an interplanar spacing of 0.548 nm. Both images reveal highly ordered single-crystalline domains without visible dislocations in the orthorhombic lattice.

Section 3: Further photodetection performance of the Bi_2S_3 phototransistor

To evaluate the broadband photodetection performance of the Bi_2S_3 phototransistor, the time-resolved photoresponse of the device was measured under periodic light on/off modulation at different excitation wavelengths (630, 525, 405, 365, and 275 nm). All measurements were carried out under identical conditions, with a fixed incident optical power of 14.34 nW, a drain-source bias of V_{ds} = 0.5 V, and a back-gate voltage of V_g = -25 V (Figure S4 and S5). As shown in Figure S4 and S5, the device exhibits highly reproducible and stable switching behavior over multiple cycles at all tested wavelengths. Moreover, the transient drain current density (J_{ds}) increases progressively as the excitation wavelength decreases from 630 to 275 nm. This wavelength-dependent photoresponse is consistent with the two mechanisms discussed in the main text. On the one hand, photons with shorter wavelengths possess higher energies, which generally lead to stronger optical excitation in Bi_2S_3. On the other hand, the hot carriers generated under short-wavelength illumination retain higher excess energy and can more readily overcome surface potential barriers before thermal relaxation, thereby contributing additional photocurrent gain, particularly in the deep-UV region. [7-8]

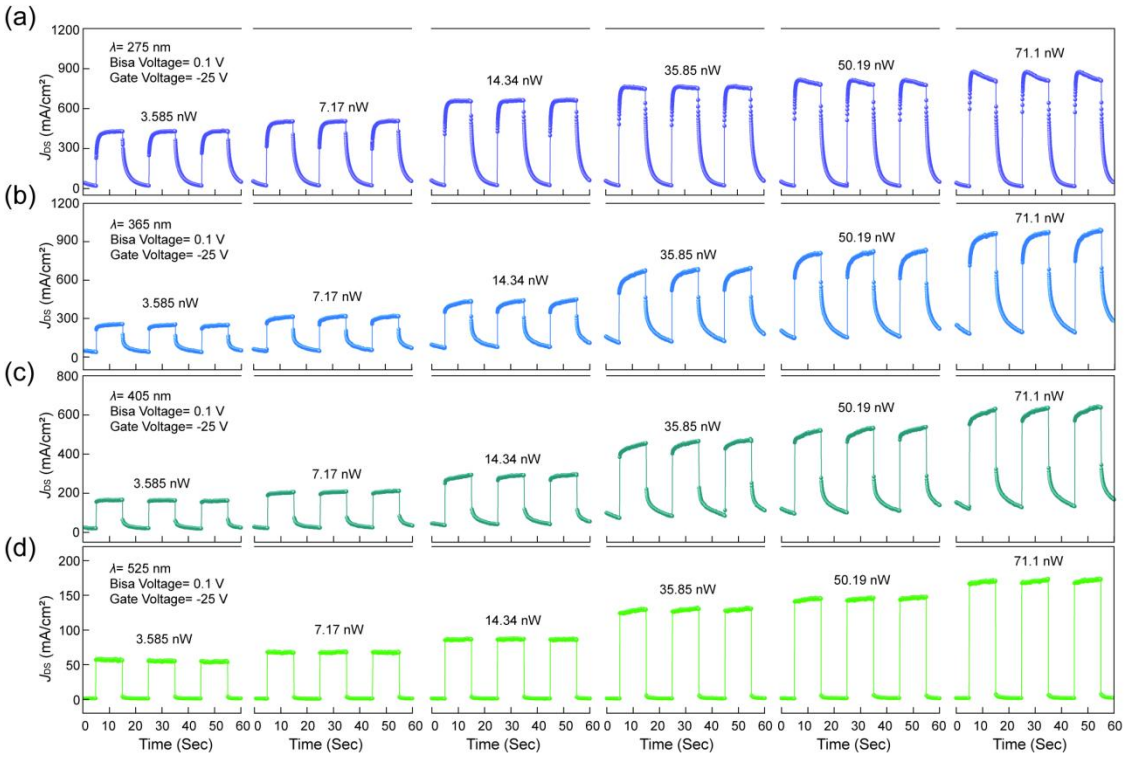

Figure S4. Transient photoresponse curves of the two-dimensional Bi_2S_3 phototransistor measured at different optical powers. Time-resolved drain current density (J_{ds}) was recorded under alternating light and dark cycles at a fixed incident wavelength, a drain-source bias of V_{ds}= 0.1 V, and a back-gate voltage of V_g = -25 V. (a) 275 nm. (b) 365 nm. (c) 405 nm. (d) 525 nm.

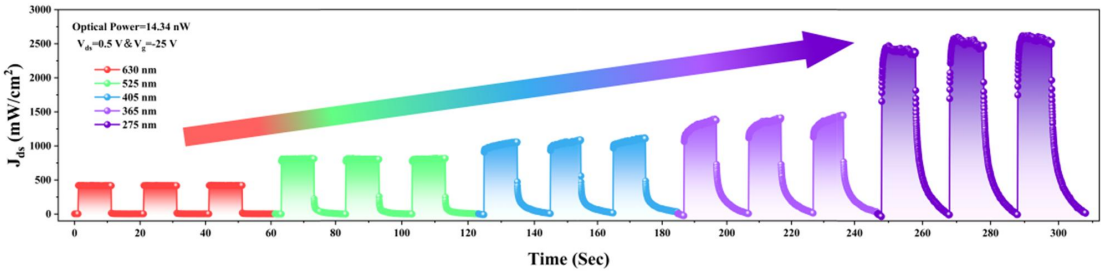

Figure S5. Transient photoresponse curves of the two-dimensional Bi_2S_3 phototransistor measured at different excitation wavelengths. Time-resolved drain current density (J_{ds}) was recorded under alternating light and dark cycles at a fixed incident optical power of 14.34 nW, a drain-source bias of V_{ds}= 0.5 V, and a back-gate voltage of V_g = -25 V. The excitation wavelength spans the range from 630 nm (red) to 275 nm (deep violet).

References

[1] He SM, Lin ZL, Lin WJ, et al. Toward large-scale CVD graphene growth by enhancing reaction kinetics via an efficient interdiffusion mediator and mechanism study utilizing CFD simulations. Journal of the Taiwan Institute of Chemical Engineers. 2021;128:400-408.

[2] S. P. Giridhar, I. H. Abidi, J. Qiu, G. Alfaza, J. O. Tollerud, P. Vashishtha, et al.Van der Waals Template-Assisted Growth of Two-dimensional Sb2S3. Adv Sci, 2025,12(46): e09903. DOI: 10.1002/advs.202509903.

[3] T. Kang, T. W. Tang, B. Pan, H. Liu, K. Zhang and Z. Luo. Strategies for Controlled Growth of Transition Metal Dichalcogenides by Chemical Vapor Deposition for Integrated Electronics. ACS Mater Au, 2022, 2(6): 665-685. DOI: 10.1021/acsmaterialsau.2c00029.

[4] Q. Ji, M. Kan, Y. Zhang, Y. Guo, D. Ma, J. Shi, et al. Unravelling Orientation Distribution and Merging Behavior of Monolayer MoS2 Domains on Sapphire. Nano Lett, 2015, 15(1): 198-205. DOI: 10.1021/nl503373x.

[5] B. M. Bersch, S. M. Eichfeld, Y. C. Lin, K. Zhang, G. R. Bhimanapati, A. F. Piasecki, et al. Selective-area Growth and Controlled Substrate Coupling of Transition Metal Dichalcogenides. 2D Mater, 2017, 4(2): 025083. DOI: 10.1088/2053-1583/aa6beb.

[6] K. Bogaert, S. Liu, J. Chesin, D. Titow, S. Gradecak and S. Garaj. Diffusion-Mediated Synthesis of MoS2/WS2 Lateral Heterostructures. Nano Lett, 2016, 16(8): 5129-5134. DOI: 10.1021/acs.nanolett.6b02057.

[7] Schaller RD, Klimov VI. High efficiency carrier multiplication in PbSe nanocrystals: implications for solar energy conversion. Physical Review Letters. 2004;92(18):186601. doi:10.1103/PhysRevLett.92.186601.

[8] Che B, Cai Z, Xiao P. Thermally driven point defect transformation in antimony selenosulfide photovoltaic materials. Advanced Materials. 2023;35:2209564. doi:10.1002/adma.202209564.